18

Hydrous Carbonatitic Liquids Drive CO_2 Recycling From Subducted Marls and Limestones

Erwin Schettino[1,2] and Stefano Poli[1]

ABSTRACT

Pelagic limestones are subducted in a variety of subduction zones worldwide. Despite the geochemical relevance of systems enriched in $CaCO_3$, previous experimental investigations mostly focused on carbonated pelites, with low Ca/(Ca+Mg+Fe) ratio. We present the compositions and the formation conditions of liquids in the model system CaO-Al_2O_3-SiO_2-H_2O-CO_2 (CASHC), building on phase relationships in the subsystems CHC and CSHC, where a second critical endpoint was suggested at temperatures as low as 515 °C, and 3.2 GPa. Multianvil experiments were performed at 4.2 and 6.0 GPa on five bulk compositions at variable Ca/Si/Al ratios. H_2O contents vary from 5.6 to 21 wt%. Aragonite + kyanite + vapor and minor lawsonite form at 700 °C, replaced by zoisite/grossular at 800 °C. Between 850 °C and 950 °C, a complex sequence of textural features is observed upon quenching of a single volatile-rich liquid phase formed at run conditions. Precipitates include dendritic $CaCO_3$, silicate glass, and Al-rich whiskers. The bulk composition of such hydrous carbonatitic liquids is retrieved by image analysis on X-ray maps, showing Ca/Si ratio increasing with pressure and temperature. Hydrous Ca-carbonatitic liquids are efficient media for scavenging volatiles from subducted crustal material and for metasomatizing the mantle wedge.

18.1. INTRODUCTION

At subduction zones, mass and heat are exchanged between different Earth reservoirs. On subduction, devolatilization of the altered oceanic crust and of serpentinized upper mantle drive the formation of mobile phases, leading to the generation of refertilized domains in the mantle wedge, capable of feeding the magmatic activity at arcs. Among subducted crustal lithologies, carbonate sedimentary rocks are heterogeneously distributed in the oceans. In modern Earth, pelagic oozes, largely constituted of calcitic nannofossils and foraminifera, ubiquitously accumulate on the seafloor above the carbonate compensation depth, except where upwelling conditions prevail and diatoms-radiolarians form siliceous oozes. Burial and plate drift are then responsible for sediment redistribution and progressive building of sedimentary covers characterized by lithological units, which are expected to maintain their compositional identity on subduction processes.

While decomposition of hydrous minerals in the slab has been thoroughly modeled to account for water-budget being recycled in arc systems (Schmidt & Poli, 2014), estimates of the magnitude of carbonate masses fed in the subduction system, and the relative efficiency of decarbonation, carbonate dissolution, and melting, driving carbon recycling, are still affected by very large uncertainties (Kelemen & Manning, 2015). Nonetheless, a global assessment of carbon dioxide and total sulphur abundances (CO_2/S_T ratio) in volcanic arc gases provides evidence for correlations between subduction of carbonate rocks and CO_2 outgassing (Aiuppa et al., 2017), thereby

[1] *Dipartimento di Scienze della Terra "Ardito Desio", Università degli Studi di Milano, Milano, Italy*

[2] *Instituto Andaluz de Ciencias de la Tierra, CSIC-Universidad de Granada, Granada, Spain*

Carbon in Earth's Interior, Geophysical Monograph 249, First Edition. Edited by Craig E. Manning, Jung-Fu Lin, and Wendy L. Mao.

suggesting the existence of processes and media capable to fractionate carbon from the uppermost geochemical reservoir of the slab. The occurrence of aragonite, and dolomite-bearing mantle xenoliths from Andean volcanoes, SW Colombia, is a direct evidence of the migration of carbon-rich metasomatic agents able to mobilize CO_2 in the upper mantle (Ferri et al., 2017). Entrainment of calcareous rocks of pelagic origin in the orogenic cycle is further documented by the occurrence of calc-schists and impure marbles, forming large tectono-stratigraphic units in mountain belts (e.g. Alps).

Despite the geochemical relevance of pelagic limestones and marls as a major carbon reservoir, experimental modeling has largely underevaluated the role of chemical systems enriched in $CaCO_3$ in sedimentary materials, and a global weighted average composition of subducted sediments (GLOSS; Plank, 2014) has been extensively used as the proxy for sedimentary contribution to the subduction factory. Experimental studies have aimed at reconstructing phase transformations on carbonated metapelites close to the composition of GLOSS (Brey et al., 2015; Grassi & Schmidt, 2011; Skora et al., 2015; Thomsen & Schmidt, 2008; Tsuno & Dasgupta, 2012). The liquid phase found on the solidus for all such compositions is silicate at $P < 5.5$ GPa, whereas carbonatitic liquids form at higher pressures (Grassi & Schmidt, 2011) or at higher temperatures, on the liquidus surface (Thomsen & Schmidt, 2008; see also Figure 11 in Schmidt & Poli, 2014). At subarc conditions, carbonatitic liquids, as efficient media for carbon transfer, are therefore restricted to relatively high temperatures (>1020 °C, Figure 18.1, unless bulk composition is enriched in Ca; Poli, 2015, 2016), and were therefore considered to be uncommon products at mature subduction zones (Syracuse et al., 2010).

Although melting of $CaCO_3$ at high pressures occurs at very high temperatures ($T > 1500$ °C at $P > 2$ GPa; Irving & Wyllie, 1975; Zhao et al., 2019, and references therein), it has long been known that water is responsible for a profound depression of the liquidus surface. Paterson (1958) documented melting of calcite in the presence of water and carbon dioxide at 930 °C, and 50 bar total vapor pressure. Wyllie and Tuttle (1959, 1960) and Wyllie and Boettcher (1969) provided the frame of reactions for the system CaO-CO_2-H_2O and experimentally demonstrated that eutectic melting occurs at temperatures down to 524 °C at 4 GPa from $CaCO_3$ + $Ca(OH)_2$ + vapor. Such an extreme influence of H_2O on melting of calcium carbonate (more than a thousand degree difference between dry and wet melting) has been recently confirmed and characterized by Foustoukos and Mysen (2015). H_2O solubility is extremely high in carbonate melts even at very low pressure; Keppler (2003) measured H_2O contents of 14 wt.% in Ca, Na, Mg carbonate melt at 900 °C, 0.22 GPa, then confirmed by qualitative estimates in

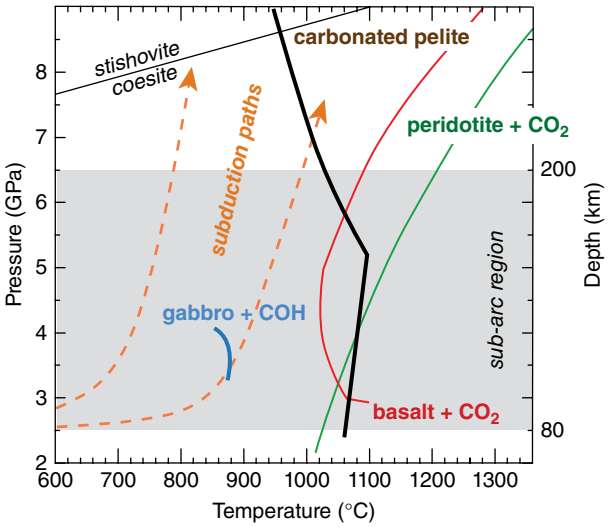

Figure 18.1 Experimentally derived reactions marking the appearance of carbonatitic liquids. The solidus on carbonated peridotite (green) is from Dasgupta & Hirschmann (2006); the solidus on carbonated basalt (red) is from Dasgupta et al. (2004). Carbonatitic liquid in carbonated pelites (brown) appears on the solidus at pressures higher than 5 GPa, whereas it exsolves on the liquidus surface at lower pressures (Thomsen & Schmidt, 2008). Hydrous carbonatitic liquids can be generated from carbonated anorthite-rich gabbros (Poli, 2015) at temperatures attained in subduction zones along slab surface (Syracuse et al., 2010). See electronic version for color representation of the figures in this book.

Foustoukos and Mysen (2015). H_2O concentrations in carbonatitic melts are four times larger than in silicate melts at conditions of diamond growth (Sokol et al., 2013; Taylor et al., 2016).

The subsolidus phase relations in the system CaO-CO_2-H_2O are characterized by carbonate dissolution in the vapor phase (for the sake of clarity, we will use here the nomenclature used by Boettcher & Wyllie, 1969) marked by the increasing solubility of $CaCO_3$ in water, with increasing pressure (Caciagli & Manning, 2003; Manning et al., 2013). There is an ample enumeration of natural records pointing to carbonate dissolution, driven by infiltrating fluids released by subducting slabs, as a mechanism relevant for CO_2 recycling at the top of the subducting slab, both at blueschist (Ague & Nicolescu, 2014) and eclogite (Frezzotti et al., 2011) facies. Carbon solubility in fluids has been shown to extend to more than 1 wt.% at pressures > 4 GPa and temperatures of 800 °C. Consequently, as the solubility of solids increases in the vapor, and that of H_2O increases in the liquid, the miscibility gap tends to shrink with increasing pressure, and a "second critical end-point" marks the appearance of a region in the phase diagram where there is compositional continuity between liquid and vapor. It is worth pointing out that such continuity is restricted to the cotectic region of the phase diagram, and

liquid + vapor still coexist as discrete phases at different compositional domains (see Figure 5 in Wyllie & Boettcher, 1969, and Figure S1 in Poli, 2015). Supercritical behavior has been proposed by Wyllie and Boettcher (1969), and Boettcher and Wyllie (1969) in the systems CaO-CO_2-H_2O and CaO-SiO_2-CO_2-H_2O, respectively.

In this study, we will test if the $CaCO_3$-rich component of subducted sediments, here modeled in the system CaO-Al_2O_3-SiO_2-H_2O-CO_2 (CASHC), is keen to promote the generation of carbonatitic liquids at sub-arc conditions, possibly at *super-critical* conditions; the mobilization of such liquids would represent an important pathway for carbon transfer from the slabs to the mantle wedge.

18.2. MODELING IMPURE MARBLES: THE SYSTEM CaO-Al_2O_3-SiO_2-H_2O-CO_2

Despite their limited thickness in comparison to the underlying altered crystalline basement, pelagic sediments concentrate large masses of carbon. As examples, DSDP site 495 on Cocos Plate, Middle America (Aubouin et al., 1982), site 504 on Nazca Plate (Cann et al., 1983), sites 212 and 260 on the Indo-Australian Plate (Heirtzler et al., 1974; von der Borch et al., 1974), and site 1124 on Pacific Plate (Carter et al., 1999) display stratigraphic columns where calcitic nannofossil oozes and chalks may constitute up to more than 90% of lithological units, with typical thicknesses of individual units in the order of tens or a few hundred meters, interbedded with minor clays, zeolites, and variable proportions of siliceous oozes. $CaCO_3$ and SiO_2 are therefore the major chemical components, where clays and zeolites introduce significant amount of Al_2O_3.

Impure marbles and calc-schists outcropping in collisional orogens constitute proxies of pelagic sediments, exhumed after high-pressure metamorphism and deformation. A large dataset of the compositions of "Schistes lustrés" and "Bündnerschiefer," representing marine sediments accumulated in alpine Tethys Ocean, is available from Garofalo (2012) and da Mommio (2018). Figure 18.2 represents the composition of marbles and calc-schists from Alpine ophiolites, and of carbonate-rich sediments from Plank and Langmuir (1998) compared to the bulk compositions adopted in experimental studies devoted to reconstruct the fate of subducted sediments at high pressure. Figure 18.2 is a chemographic projection built on the basis of phase assemblages predicted by thermodynamic calculations. Pseudosections (not shown) were calculated following the approach of Connolly (1990), using the internally consistent thermodynamic dataset and the CORK equation of state for fluids of Holland and Powell (2011), implemented by the carbonate solution model by Franzolin et al. (2011) and aragonite properties by Zhao et al. (2019). Calculated

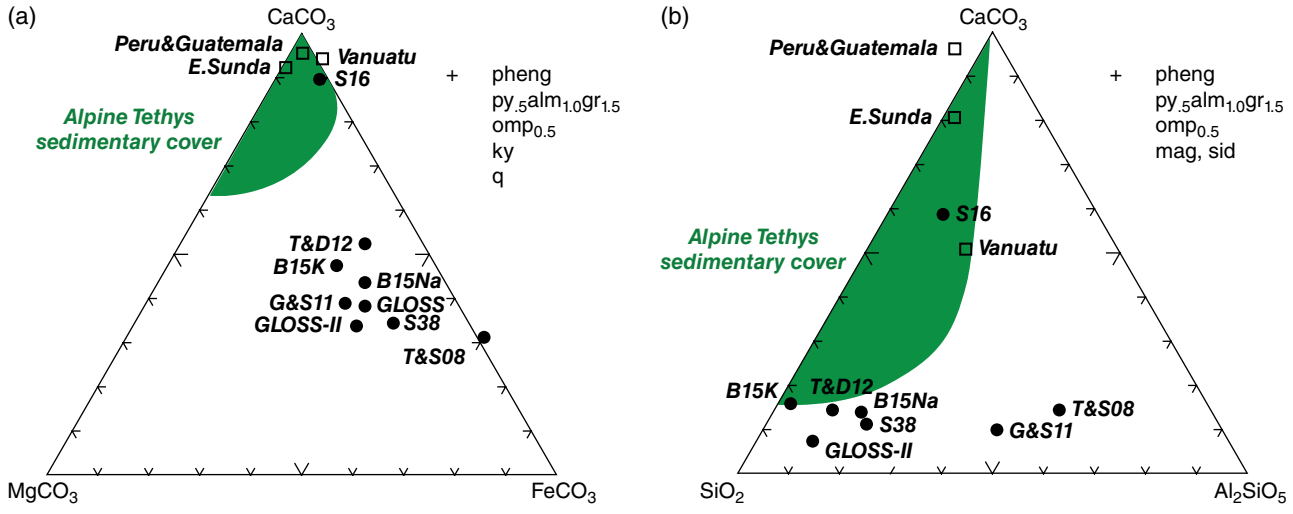

Figure 18.2 Chemographic representation of carbonated sedimentary materials in the system $CaCO_3$-$MgCO_3$-$FeCO_3$ (a) and $CaCO_3$-SiO_2-Al_2SiO_5 (b), projected from garnet, omphacite, phengite, and quartz + kyanite in (a), and magnesite + siderite in (b). The green field stands for the compositional variation of impure marbles, carbonate-silicate rocks, and calc-schists from the ophiolitic suites in the Alps (Garofalo, 2012; da Mommio, 2018). Squares are the average compositions of calcite-rich sedimentary units being subducted at Sunda, Vanuatu, Peru, and Guatemala (Plank & Langmuir, 1998). Filled circles show the bulk compositions of starting materials used in experimental studies: T&S08 = Thomsen & Schmidt (2008); G&S11 = Grassi & Schmidt (2011); T&D11 = Tsuno & Dasgupta (2012); B15K and B15Na = Brey et al. (2015), K- and Na-enriched, respectively; S16 and S38 = Skora et al. (2015), bulk composition 144-16 and 144-38, respectively. GLOSS and GLOSS II from Plank (2014). See electronic version for color representation of the figures in this book.

phase proportions are dominated by aragonite, ranging from 40 wt.%, in calc-schists, and 70 wt.% in impure marbles. The abundance of Na_2O and K_2O controls the amount of omphacite$_{s.s.}$ and white mica, respectively, over a wide range of P-T conditions. The main hydrous minerals that occur are lawsonite and zoisite, their breakdown responsible to form garnet + kyanite + coesite + H_2O. At pressures higher than ~4 GPa, aragonite coexists with minor magnesite. On the basis of the general features of calculated pseudosections, Figure 18.2 is therefore constructed projecting from garnet ($Mg_{0.5}Fe_{1.0}Ca_{1.5}Al_2Si_3O_{12}$), omphacite ($Na_{0.5}Ca_{0.5}[Mg,Fe]_{0.5}Al_{0.5}Si_2O_6$), and phengitic mica ($K[M,Fe]_{0.3}Al_{1.7}Al_{0.7}Si_{3.3}[OH]_2O_{12}$), plus Al_2SiO_5 and silica in Figure 18.2a, and $(Mg,Fe)CO_3$ in Figure 18.2b. Figure 18.2 shows that bulk composition used in the experiments of Thomsen and Schmidt (2008), Tsuno and Dasgupta (2012), Grassi and Schmidt (2011), Skora et al. (2015) (bulk 144-38), and Brey et al. (2015) are characterized by low Ca/(Ca+Mg+Fe) ratio and high SiO_2+Al_2O_3, similarly to the model GLOSS (Plank & Langmuir, 1998). Only bulk composition 144-16 in Skora et al. (2015) is representative of pelagic sediments discussed here.

Although the composition of garnet, omphacite, mica, and (Mg,Fe)-carbonate will vary at different P-T, a common feature of this family of marine sediments is the predominance of $CaCO_3$, and a more or less pronounced saturation in silica and Al_2SiO_5. Phase relationships explored in this experimental work are then modeled in the five-components system, CaO-Al_2O_3-SiO_2-CO_2-H_2O, on five different bulk compositions with three variable Al_2O_3/SiO_2 ratios, in order to stabilize, at high pressure, aragonite + coesite + an alumino-silicate phase such as garnet, zoisite or kyanite, depending on pressure and temperature conditions. Silica saturation and addition of alumina are expected to prevent the crystallization of dellaite and portlandite, experimentally recorded on the eutectic of the system CaO-SiO_2-CO_2-H_2O (Boettcher & Wyllie, 1969). The amount of volatile components were defined over different CO_2:H_2O ratios, so that phase relationships between a low-density vapor, solute-rich vapor, volatile-rich liquid, and, possibly, supercritical liquid were explored, at different P-T conditions, over a wide compositional range.

18.3. EXPERIMENTAL AND ANALYTICAL METHODS

Experiments were performed with mixtures of crystalline powders plus distilled water, when required. Reagent grade $CaCO_3$ calcite, amorphous silica, $Al(OH)_3$, and synthetic zoisite were used as starting materials. The $Al(OH)_3$ was employed as a source of alumina, and of H_2O for bulk 1 and 1b (Table 18.1), in order to favor reaction kinetics at relatively low temperature. Bulk compositions were constructed to lie close to the compositional pseudosection $CaCO_3$–H_2O as projected from Al_2SiO_5 and SiO_2, and were therefore at a constant CaO:CO_2 ratio but variable $CaCO_3$:H_2O ratio (molar fractions of components in Table 18.1). Bulk compositions were then obtained by mixtures of calcite + $Al(OH)_3$ + amorphous silica (bulk 1 and 1b), calcite + zoisite + water (bulk 2), and calcite + zoisite + silica + water (bulk 3 and bulk 3b). Capsules were made of Au tubing, 3.0 mm outer diameter, and loaded with ~7 mg of solids and up to 1.5 microliter of water, if any; accuracy in H_2O addition by water is in the order of 7%, whereas <1% when $Al(OH)_3$ is used. All capsules were welded after loading the starting materials, previously permanently stored in a vacuum oven at 110 °C. Distilled water was added at the bottom of the run charge by using a high-precision microsyringe. In order to prevent water loss, capsules were held into a frozen steel support during welding.

Table 18.1 Bulk composition of starting materials.

	1	1b	2	3	3b
CaO	40.02	35.08	38.46	35.70	42.15
Al_2O_3	13.00	10.41	4.81	4.47	3.91
SiO_2	8.58	21.38	6.08	12.82	16.09
CO_2	31.41	27.53	27.17	25.22	30.64
H_2O	7.00	5.60	23.48	21.80	7.22
Total	100.00	100.00	100.00	100.00	100.00
X_{CaO}	0.274	0.257	0.182	0.162	0.290
X_{CO2}	0.274	0.257	0.166	0.146	0.268
X_{H2O}	0.299	0.256	0.606	0.618	0.309
$X_{Al2SiO5}$	0.147	0.126	0.033	0.033	0.045
X_{SiO2}	0.006	0.104	0.013	0.041	0.088

Note. Oxides in wt%; components in molar fractions: X_{CaO} = CaO/(CaO+CO_2+H_2O +Al_2SiO_5+SiO_2).

Experiments were performed using a Walker-type multianvil apparatus on a 1000 ton press at the Dipartimento di Scienze della Terra, Università degli Studi di Milano. WC cubes had edge lengths of 32 mm and truncation edge lengths of 17 mm. Assemblies were composed by pyrophyllite gaskets, a prefabricated MgO-octahedron (containing 5 wt% Cr_2O_3) with 25 mm edge length, and cylindrical graphite heater. A MgO sleeve was placed between capsules and graphite. The axial thermocouple (Pt- $Pt_{90}Rh_{10}$, S-type) was placed in direct contact with the capsules, and a mullite thermocouple ceramic was used. Thermal gradients over the length of the capsule in this relatively large assembly are less than 20 °C–30 °C at experimental temperatures of 700 °C–1000 °C. Pressure calibration for the 25 M assembly was performed at 1000 °C by using the coesite-stishovite and $CaGeO_3$ garnet-perovskite phase transitions, occurring respectively at 8.7 GPa (Zhang et al., 1996) and 6.1 GPa (Susaki et al., 1985), with uncertainties of about ±3%.

Our study assumes that redox reactions are negligible, on the basis of relatively low permeability of gold to hydrogen (Chou, 1986), and of absence of precipitation of graphite, as verified by XRPD on selected run charges. Therefore, vapor composition is expected to adjust internally in order to minimize the free energy of the reactive system (see also Poli & Schmidt, 1998).

At the end of the experiments, recovered capsules were longitudinally embedded in epoxy resins. Sample mounts were ground by using ethanol, instead of water, in order to avoid dissolution of the quench phases. After exposing the very first portion of the run charge, the capsules were impregnated under vacuum with low-viscosity epoxy resin. The samples were later polished with a 1 μm diamond paste, and finally carbon coated for scanning electron microprobe (SEM) analysis. Textural and compositional characterizations were performed using a WDS-equipped JEOL JXA8200 electron microprobe analyzer (EMPA). Analytical conditions were set to 15 kV acceleration voltage, and 5 nA current for a less than ~1 μm spot-size beam. Defocused beam was used whenever possible. X-ray elemental maps on experimental products were acquired with a 0.3 μm step-size and 20 ms time acquisition for each element. Standards used are anorthite USNM137041 for aluminum, and wollastonite for calcium and silicon.

18.4. RESULTS

18.4.1. Microstructural Analysis

A total of 13 successful experiments were performed between 700 °C and 950 °C at two pressures, 4.2 and 6 GPa. Run conditions, starting materials, duration of the experiments, mineralogical assemblages, and microstructural features of quench products are reported in Table 18.2. The attainment of textural equilibrium at run conditions was recognized by the development of polygonal grain boundaries, and 120° triple junctions between the solid phases.

The existence of a mobile, volatile-rich, phase at the P-T conditions of the experiments was determined based on microstructural criteria. The occurrence of vapor and solute-rich vapor are expected to produce a diffuse porosity, provided the relatively high proportions of H_2O available. Carbonatitic liquids are characterized by low dihedral angle (<30°; Minarik & Watson, 1995; Watson

Table 18.2 Summary of the experiments and of the run products.

Run	Bulk	P (GPa)	T (°C)	t (h)	Starting Materials	Min. Assemblage	Quench Products
SPCC1	1	4.2	700	81	cc + $Al(OH)_3$ + si	ky + law + ar	—
SPCC2	1	4.2	800	72	cc + $Al(OH)_3$ + si	ky + ar	cc-drop si-drop al-whisk
SPCC4	1	4.2	850	62	cc + $Al(OH)_3$ + si	cor + zo (ky) + ar	cc-dend al-whisk
SPCC5	1b	4.2	850	110	cc + $Al(OH)_3$ + si	coe + zo (ky) + ar	cc-film si-drop al-whisk
SPCC9	3	4.2	850	122	cc + zo + si + w	coe + gr (zo) + ar	cc-dend si-drop al-whisk
SPCC14	3b	4.2	850	120	cc + zo + si + w	coe + gr (zo) + ar	glass cc-drop
SPCC3	1	4.2	900	83	cc + $Al(OH)_3$ + si	cor + zo (ky) + ar	cc-dend si-drop al-whisk
SPCC6	1b	4.2	900	49	cc + $Al(OH)_3$ + si	coe + zo + ar	cc-dend si-drop al-whisk
SPCC7	2	4.2	900	120	cc + zo + w	cor + gr (zo) + ar	cc-dend si-drop al-whisk
SPCC8	3	4.2	900	79	cc + zo + si + w	gr (zo) + ar	cc-dend glass
SPCC13	3b	4.2	900	113	cc + zo + si + w	coe + gr + ar	cc-dend si-drop glass
SPCC10	3	6	900	118	cc + zo + si + w	coe + gr (zo) + ar	cc-dend si-drop al-whisk
SPCC11	3	6	950	89	cc + zo + si + w	coe + gr (zo) + ar	cc-dend si-glob glass

Note. Phase abbreviations: cc = calcite; si = amorphous silica; zo = zoisite; w = water; ky = kyanite; law = lawsonite; ar = aragonite; gr = grossular; coe = coesite; cc-drop = droplets of $CaCO_3$; si-drop = droplets of SiO_2; al-whisk = Al-Si-rich whiskers; cc-dend = dendrites of $CaCO_3$.

et al., 1990), and they are expected to fractionate at the hot portion of the capsule, by Soret thermal diffusion, related to thermal gradient in the multianvil assembly. Carbonatitic liquids cannot be quenched to a glass, because of extremely low viscosities (Genge et al., 1995; Kono et al., 2014), and melting of the system can be inferred by the development of crystal morphologies that are indicative of textural disequilibrium due to rapid cooling rates, such as tabular, skeletal, branching, chain, feather-like, dendritic, spherulitic textures (at increasing cooling rates, or undercooling steps; Donaldson, 1976; Lofgren, 1974). Spherulites, and spherical droplets ("fish eggs" in Skora et al., 2015), can be the result of precipitation of amorphous solid material exsolved from the hydrous vapor into insoluble colloidal particles.

In the occurrence of coexisting vapor and liquid at run conditions, vapor bubbles are expected to coalesce into very few, large, subspherical bubbles, again as a result of low viscosity of the liquid. The presence of diffuse microvesicles within quench material can be attributed to the exsolution of volatile components during cooling, from a volatile-rich liquid present at high pressure/high temperature (e.g. see Figure 2 in Thomsen & Schmidt, 2008).

At 700 °C, 4.2 GPa, in bulk composition 1, the mineralogical assemblage is defined by aragonite + lawsonite + kyanite. Aragonite is organized in an equigranular polygonal texture, characterized by 120° triple junctions, while kyanite occurs in aggregates of tabular crystals. A diffuse interstitial porosity in the capsule testifies to the presence of a vapor phase coexisting with the solid assemblage. At 800 °C, 4.2 GPa, bulk 1, pores contain spherical droplets, whiskers, and spherulites of radially arranged fibers. All such disequilibrium textures are attained during rapid crystal growth for large steps of undercooling, therefore testifying to the presence of a solute-rich vapor at run conditions. Spherical droplets are both silicatic (Figure 18.3a) and calcitic (Figure 18.3b), while whiskers are relatively alumina rich (see section 18.4.2). Interestingly, silica droplets occur at the tip end of whiskers, suggesting the former precipitates late in the sequence. The solid assemblage (Figure 18.4a) shows that lawsonite is no longer present, and the assemblage aragonite + zoisite + kyanite is stable. Phase assemblages shown in Figure 18.4, calculated from thermodynamic data, should be regarded as schematic because the projection assumes a free binary vapor, for simplicity.

At 850 °C and 4.2 GPa (Figure 18.3 c, d, and e), run products display a larger proportion of silicate and carbonate material precipitated on quenching, suggesting that the vapor phase becomes increasingly solute enriched with increasing temperature. At 850 °C, bulk compositions 1, 1b, and 3, we observe the precipitation of dendritic carbonates, of intergranular films composed of $CaCO_3$ between aragonite grain boundaries, and of $CaCO_3$ whiskery overgrowths. Precipitates also include Al-enriched whiskers and a large proportion of silica droplets and spherulites. Since the observed textures do not provide any evidence for a biphasic coexistence of vapor and melt, the transition from a low-density to a solute-rich liquid should be regarded as the result of the progressive increase in solubility of both carbonates and silicates in the "fluid" phase, with increasing temperature. In the frame of a continuous transition from vapor to liquid, the microstructural criterion used to highlight the appearance of a liquid-like phase is based on the assumption that crystal habits (from bladed, to chain, to feathery, see Donaldson 1976) develop when the mobile phase, quenched at rates typical of multianvil assemblies (ΔT ~300 °C–400 °C/sec), is characterized by a framework favoring growth. Dendrites of calcite were observed to form on quenching hydrous $CaCO_3$ melt (Paterson, 1958). In bulk composition 1, the mobile phase coexists with a solid assemblage defined by aragonite + zoisite + corundum (Figure 18.4b) organized in polygonal texture, while kyanite only appears as inclusions in zoisite crystals. In bulk composition 1b (derived from silica addition), the solid assemblage is aragonite + zoisite + coesite. In bulk composition 3, aragonite develops polygonal textures and planar grain boundaries along with grossular and coesite, while zoisite only occurs as inclusions in poikilitic grossular. In bulk 3b, characterized by a low H_2O/SiO_2 ratio, a silicate glass forms. Subspherical blebs of $CaCO_3$ precipitate embedded in the silicate glass (Figure 18.3e), suggesting that immiscibility between a silicate and carbonatitic liquid might have occurred at run conditions. However, immiscibility in alkali free systems is questionable, and it will not be discussed further in this work.

At 900 °C and 4.2 GPa, run products in all experiments are characterized by the presence of a *meniscus* at the top of the capsule marked by a sharp boundary between a complex intergrowth of dendrites, droplets, spherulites, and glass, and a polygonal aggregate of coarse grains (Figure 18.3 f, g). This texture is interpreted as evidence of a hydrous carbonatitic liquid segregating at the hot top of the capsule. Large, spherical bubbles were never observed, suggesting that volatiles are entirely dissolved in the liquid and no vapor coexists with such liquid at run conditions. In bulk composition 1, the solid assemblage is aragonite + zoisite + corundum (Figure 18.4c), while kyanite occurs as inclusions in zoisite. A large proportion of calcium carbonates precipitated in a dendritic texture, characterized by rhombohedral intergrowths of acicular and chain-like crystals of $CaCO_3$ (Figure 18.3 g, h, i), with Al-rich whiskers radially arranged to form spherulite-like morphologies. The outer shell of the spherules is built of silica droplets precipitated at the tips of the

whiskers (Figure 18.3h). In bulk composition 2, solid assemblage includes aragonite + grossular + corundum, and zoisite occurs as inclusions in poikilitic grossular. In bulk 3 (run SPCC8), the solid assemblage is defined by aragonite + grossular. Despite the large fraction of H_2O in the starting material for bulk 3 (~21 wt.%), there is no textural evidence for a vapor phase coexisting with the liquid at run conditions. On the contrary, glass is

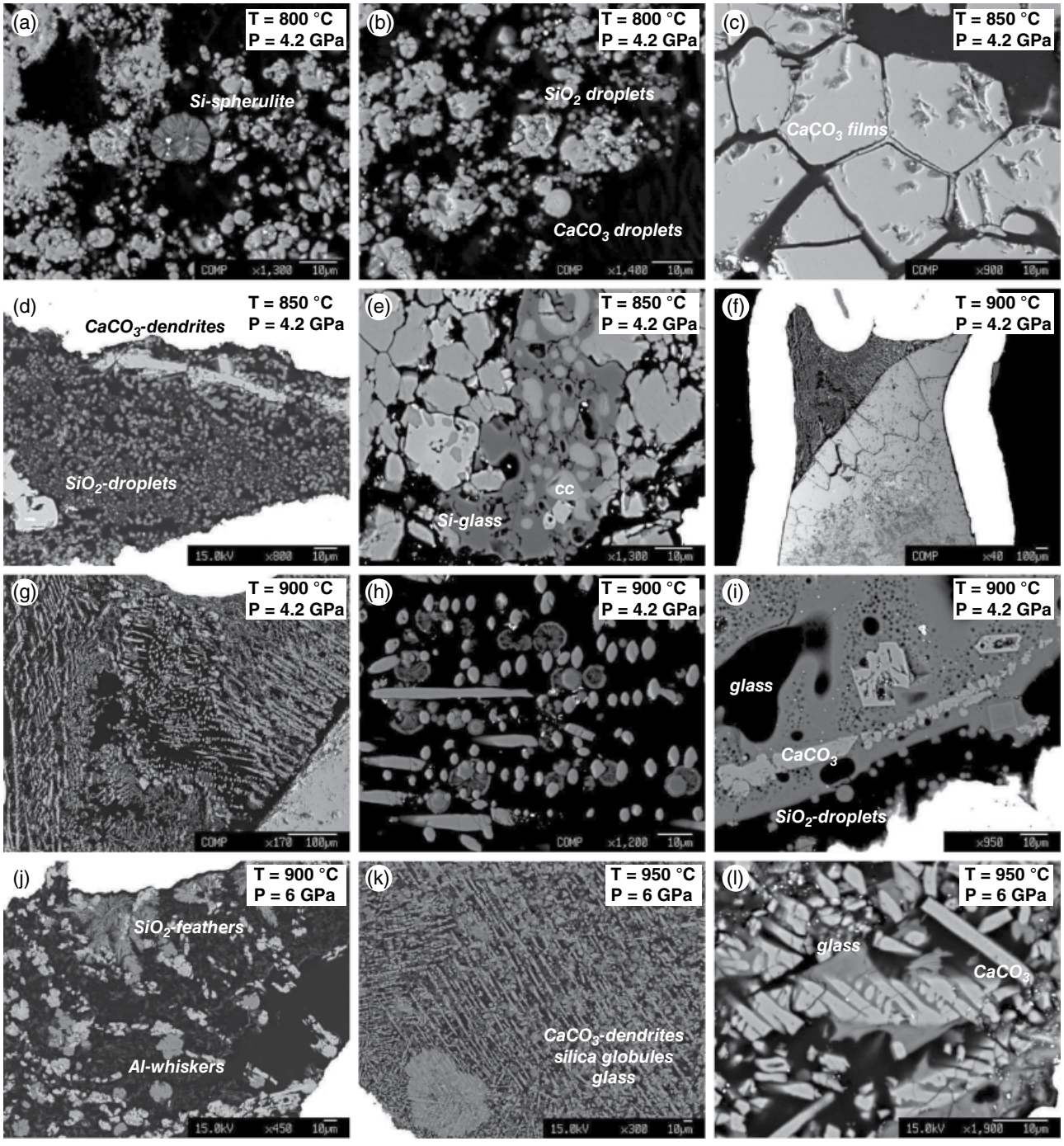

Figure 18.3 Back-scattered electron images on representatives run products: (a) and (b) 4.2 GPa, 800 °C, bulk 1 run SPCC2 (see Table 18.2); (c) 4.2 GPa, 850 °C, bulk 1b, run SPCC5; (d) 4.2 GPa, 850 °C, bulk 3, run SPCC9; (e) 4.2 GPa, 850 °C, bulk 3b, run SPCC14; (f), (g), and (h) 4.2 GPa, 900 °C, bulk 1, run SPCC3; (i) 4.2 GPa, 900 °C, bulk 3b, run SPCC13; (j) 6 GPa, 900 °C, bulk 3, run SPCC 10; (k) and (l) 6 GPa, 950 °C, bulk 3, run SPCC11. See electronic version for color representation of the figures in this book.

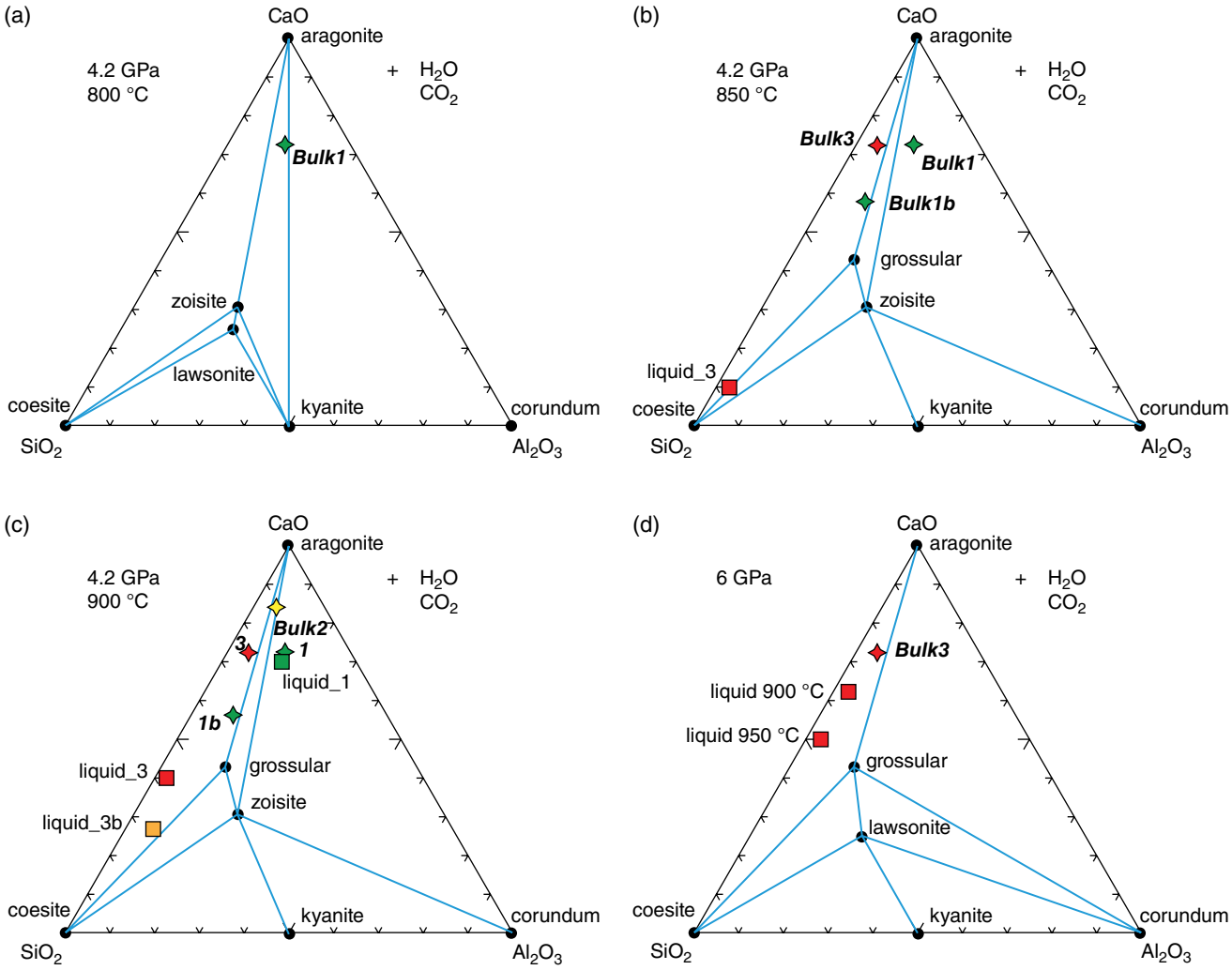

Figure 18.4 Isobaric and isothermal composition diagrams for the system CaO-Al_2O_3-SiO_2-CO_2-H_2O, projected from H_2O and CO_2. Phase assemblages are calculated using thermodynamic data in Holland & Powell (2011) and aragonite properties in Zhao et al. (2019). Diamonds are the bulk compositions investigated here. Note that bulk 3 and 3b differ by H_2O content only. Squares refer to the compositions estimated for the liquid reconstructed from image analysis. See electronic version for color representation of the figures in this book.

recovered, most probably as a result of the high silica proportion in bulk 3. Glass is highly fragmented and vesiculated, as a result of the exsolution of volatile components during quench. Run products on a bulk 3b, with lower H_2O contents (~7 wt. %), include aragonite, grossular, and coesite. Again, the liquid precipitates dendritic carbonates scattered on a glassy, fragmented groundmass characterized by diffuse, small vesicles (Figure 18.3i).

A set of experiments was performed at 6 GPa, at 900 °C and 950 °C, on bulk composition 3. The solid assemblage in this range of P-T is aragonite + grossular + coesite, with inclusions of relic zoisite in poikilitic grossular. At 900 °C, quench products are characterized by an intergrowth of feathery silicates, dendritic carbonate, Al-Si rich spherulites and whiskers (Figure 18.3j). At 950 °C, the segregated liquid precipitates a larger amount of dendritic carbonates, with elongated skeletal and chain-type morphologies, arranged in a rhombohedral intergrowth. Fragmented glass is observed (Figure 18.3 k and l), and poikilitic silica globules include the other components, thus completing the precipitation sequence.

18.4.2. Chemistry of Precipitates and Composition of the Liquid

Since individual solid particles precipitated on quenching are very fine grained, electron probe microanalyses provide a semi-quantitative determination of their chemistry. Therefore, totals reported in Table 18.3 should not be considered entirely compensated by H_2O and CO_2, probably present in all precipitates. The composition of the vapor phase after quench unlikely reflects the H_2O/CO_2

Table 18.3 Composition of quench products (in wt.%).

Run	SPCC3		SPCC8		SPCC9		SPCC10		SPCC11		SPCC13	
P (GPa)	4.2		4.2		4.2		6		6		4.2	
T (°C)	900		900		850		900		950		900	
Bulk	1		3		3		3		3		3b	
	mean	*±σ*	*mean*	*±σ*	*mean*	*±σ*	*mean*	*±σ*	*mean*	*±σ*	*mean*	*±σ*
Droplets												
CaO	0.63	0.13	-	-	0.85*	0.19*	0.31	0.05	3.1	1.79	0.77	0.11
Al_2O_3	2.51	1.68	-	-	2.38*	0.18*	0.98	0.37	3.43	0.66	1.85	0.75
SiO_2	64.06	11.80	-	-	93.32*	3.79*	91.13	3.58	86.97	2.79	88.67	6.58
Total	67.47	13.27	-	-	96.55*	4.11*	92.42	3.61	93.49	1.64	91.29	7.43
X_{Ca}	0.01		-		0.01*		0.00		0.04		0.01	
X_{Si}	0.95		-		0.96*		0.98		0.92		0.97	
X_{Al}	0.04		-		0.03*		0.01		0.04		0.02	
Whiskers												
CaO	0.69	0.47	-	-	-	-	0.32	0.07	-	-	-	-
Al_2O_3	42.96	21.99	-	-	-	-	12.95	4.59	-	-	-	-
SiO_2	38.27	13.88	-	-	-	-	27.56	9.80	-	-	-	-
Total	83.12	9.95	-	-	-	-	40.83	14.62	-	-	-	-
X_{Ca}	0.01		-				0.01		-		-	
X_{Si}	0.45		-		-		0.64		-		-	
X_{Al}	0.54		-		-		0.35		-		-	
Glass												
CaO	-	-	10.85	0.04	-	-	-	-	11.21	4.78	6.42	1.40
Al_2O_3	-	-	2.49	0.14	-	-	-	-	7.24	3.52	4.74	1.38
SiO_2	-	-	59.19	2.81	-	-	-	-	49.01	8.00	61.35	10.02
Total	-	-	72.52	2.96	-	-	-	-	67.46	6.62	72.72	10.11
X_{Ca}	-		0.16		-		-		0.17		0.10	
X_{Si}	-		0.80		-		-		0.70		0.83	
X_{Al}	-		0.04		-		-		0.12		0.08	

Note. X_{Ca} = Ca/(Ca+Si+Al); X_{Si} = Si/(Ca+Si+Al); X_{Al} = Al/(Ca+Si+Al).

ratio in the mobile phase at run conditions. Equation of states for C-O-H fluids by traditional thermodynamic modeling using mixing properties of H_2O and nonpolar species (e.g. Holland & Powell, 1991) predict low CO_2/(H_2O+CO_2) (<0.9) up to 900 °C (see Figure 7 in Poli & Schmidt, 1998). However, complexities in the speciation of complex fluids dissolving both silicates and carbonates (Tumiati et al., 2017; Facq et al., 2016) hinder a reliable estimate of the speciation of volatile species in the investigated liquids at run conditions. Estimates of H_2O-CO_2 abundance in the mobile phase by mass balance would require an estimate of the volume of the mobile phase with respect to solids, but in most experiments vapor/liquid segregates at the hot end of the capsule. Therefore, unless a 3D image is acquired, it is impossible to quantify its volume, and from that to try to reconstruct the relative proportions of voids (volatiles), quench products, and equilibrium solids. We will therefore discuss hereafter the composition of liquids in terms of Ca/Si/Al ratios.

Carbonate particles (spherules, dendrites, chains, whiskery overgrowths) invariably show Ca as the unique cation detected by EPMA (other than carbon, not quantified here), and they are therefore assumed to be $CaCO_3$ in composition. Silica-rich droplets are characterized by Si/(Ca+Si+Al) (X_{Si}) > 0.9, and glass exhibits a wider compositional range, although mean values converge on X_{Si} = 0.7–0.8, X_{Ca} = 0.10–0.17, and X_{Al} = 0.04–0.12. Whiskers grossly fall midway between Si and Al, testifying to significant fractionation of alumina in this phase.

WDS X-ray elemental maps on segregated precipitate intergrowths at the top capsule were acquired at a step size of 0.3 micrometers in order to determine the relative proportions of particles. Image analysis was performed using a customized routine developed as a Mathematica© notebook. The composition of the liquids in terms of Ca, Si, and Al (Table 18.4) was estimated by summing the weighted contribution of carbonate, glass, whiskers, and droplets. Although densities are unknown, we assume that silica droplets have a density in the order of 2/3 that of carbonate, in order to limit carbonate underestimation, which is probably unavoidable, as H_2O is likely to be

Table 18.4 Volume abundance of quench products (as percentage of the total) and reconstructed liquid compositions (in wt.%).

Run	SPCC3	SPCC8	SPCC9	SPCC10	SPCC11	SPCC13
P (GPa)	4.2	4.2	4.2	6	6	4.2
T (°C)	900	900	850	900	950	900
Bulk	1	3	3	3	3	3b
Calcium carbonate	76%	30%	10%	61%	47%	22%
Silica droplets	10%	-	90%	29%	35%	-
Al whiskers	17%	-	-	10%	17%	-
Glass	-	70%	-	-	-	78%
Liquid						
CaO	69.8	38.7	9.7	61.0	48.4	25.4
Al_2O_3	12.4	2.4	2.2	2.7	3.4	5.3
SiO_2	17.8	58.9	88.1	36.3	48.2	69.3

present in both silica-rich droplets as well as in Si-Al whiskers. Even a gross estimate of liquid abundance, and therefore (by mass balance) of total volatiles in the liquid, is further hampered both by the irregular geometry of the meniscus relative to capsule walls, and by difficulty in estimating the actual porosity of the run charge after quench. Nonetheless, assuming that a single volatile-rich phase forms, and that H_2O initially added in the starting material strongly fractionates in the segregated liquid, all liquids should contain more than approximately 30–40 wt.% H_2O.

At 850 °C and 4.2 GPa, it was not possible to clarify from textural evidence whether a solute-rich vapor phase, or volatile-rich liquid already formed. In both cases, as previously stated, we have no indication for two coexisting mobile phases in this run, and the composition of the "liquid" is included in Table 18.4 and plotted in Figure 18.4b. With increasing temperature, the amount of solute content increases, as estimated qualitatively from image analysis, and a larger fraction of calcium carbonate precipitates, leading to a relative enrichment in Ca in Figure 18.4 c and d. It is worth pointing out that it is possible to reconstruct relative abundances only. As a consequence, relative silica enrichment as observed in liquids at 4.2 GPa, 900 °C at bulk 3 or 3b (coesite-bearing) does not imply that absolute amount of dissolved $CaCO_3$ (and then precipitated) is lower than at bulk 1 (corundum-bearing). The experiments performed at 6 GPa suggest an increase in carbonate dissolution and precipitation; however, silicate glass is formed at 6 GPa and 950 °C, but not at 900 °C. This might indicate that isopleths representing silicate dissolution should have a positive dP/dT slope, whereas carbonate dissolution has steeper or negative dP/dT slopes. This is grossly consistent with what is expected from solubility models of $CaCO_3$ and SiO_2 in aqueous fluids at high temperatures and pressures in the coesite field (Caciagli & Manning, 2003; Connolly & Galvez, 2018; Manning, 1994).

18.5. HYDROUS-CARBONATITIC LIQUIDS FORM AT SUB-ARCS

Subducted pelagic carbonates can be modeled as a simple mixture of predominant $CaCO_3$ (nannofosils and foraminifera), minor flint (diatoms, radiolarians), and pelagic clay. The "White Cliffs of Dover" are the most popular example of such a sedimentary sequence. If dry conditions prevail, eutectic melting of calcite, wollastonite, and quartz occurs at temperatures higher than 1300 °C (Huang et al., 1980), therefore indicating that subduction promotes recycling of aragonite into the deep mantle (Figure 18.5). However, most relevant at subduction zones, serpentinized ultramafic lithosphere and altered oceanic crust are known to extensively dehydrate at sub-arc conditions and to release aqueous vapors flushing the slab to mantle interface (Schmidt & Poli, 2014), where calcitic/aragonitic marbles occur.

H_2O strongly depresses the melting temperature of $CaCO_3$ and the wet solidus in $CaO\text{-}CO_2\text{-}H_2O$ should be in equilibrium with portlandite. Addition of silica (a ubiquitous minor component in limestones, and a major solute in high pressure vapors) introduces numerous mineral phases potentially present: dellaite $Ca_6Si_3O_{11}(OH)_2$, spurrite $Ca_5(SiO_4)_2(CO_3)$, calciochondrodite $Ca_5(SiO_4)_2(OH)_2$, scawtite $(Ca_7Si_6(CO_3)O_{18}\bullet 2(H_2O)$, tilleyite $Ca_5Si_2O_7(CO_3)_2$ (Boettcher & Wyllie, 1969; Grice, 2005; Liu & Lin, 1995). Such minerals are rare in nature, or overlooked in high-pressure rocks and experimental studies. Boettcher and Wyllie (1969) proposed, on experimental basis, that eutectic melting of hydrous Ca-silicate + $CaCO_3$ + $Ca(OH)_2$ + vapor occurs at very low temperatures and that the second critical end point in the system

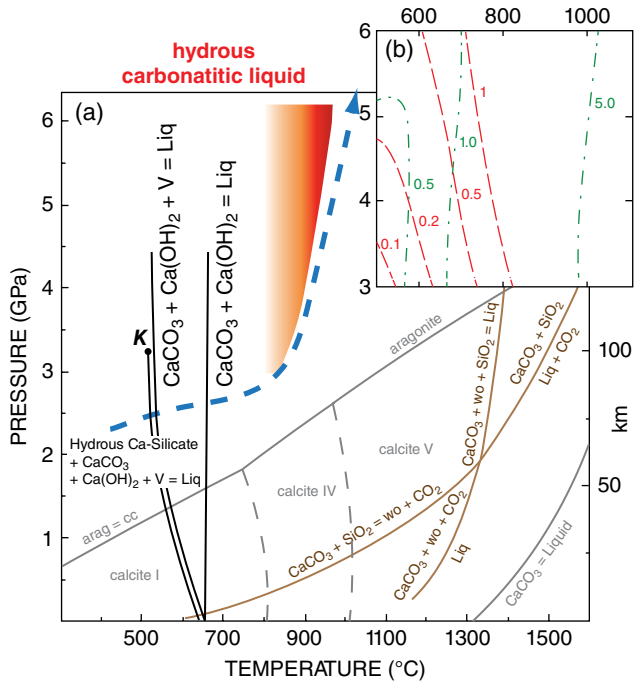

Figure 18.5 (a) Univariant phase relationships, and melting curves, experimentally determined for the systems $CaCO_3$ (gray; Zhao et al., 2019), CaO-SiO_2-CO_2 (brown; Huang et al., 1980), and CaO-SiO_2-H_2O-CO_2 (black; Wyllie & Boettcher, 1969; Boettcher & Wyllie, 1969). *K* refers to the second critical end point determined in the system CSHC (Boettcher & Wyllie, 1969). The red field represents the condition for generation of hydrous carbonatitic liquids from this study, compared to the P-T path for a slab surface in a warm-type subduction regime (thermal model D80 from Syracuse et al., 2010). (b) Red dashed lines are contours of carbon concentration in weight percent for aqueous fluids saturated in $CaCO_3$ (Kelemen & Manning, 2015); green dashed-dotted lines are contours of total Si molality in aqueous fluid (Connolly & Galvez, 2018). See electronic version for color representation of the figures in this book.

CaO-SiO_2-H_2O-CO_2 is located at 515 °C and 3.2 GPa (Figure 18.5), at low $CO_2/(H_2O+CO_2)$. Whether or not this model system is relevant for predicting the behavior of subducted marbles, hydrous carbonatitic liquids are potentially feasible at pressure-temperature conditions routinely attained at the top of subducting slabs (Syracuse et al., 2010).

Clay minerals (ideally $Al_2Si_2O_5[OH]_4$ in the model system investigated here) provide a source of Al_2O_3 to form grossular and kyanite, and of H_2O to form lawsonite, and zoisite, able to promote vapor or liquid on devolatilization. Saturation in silica and in Al-silicates for experiments performed here is observed to prevent the formation of portlandite and of phases recovered in the Al-free system, and most notably causes a shift of the liquidus surface. A diffuse porosity, to be ascribed to a vapor phase, is present at 800 °C, almost 300 °C above the supercritical liquid predicted in the system CaO-SiO_2-CO_2-H_2O. Vapor at 4 GPa, 800 °C is predicted to have a $CO_2/(H_2O+CO_2)$ = 0.02 on a thermodynamic basis (Poli & Schmidt, 1998), very similar to what is expected at the second critical end point in the system CSHC. Because evidence of liquid is recovered only from 850 °C, a compositional/thermal barrier necessarily exists between the liquidus surface found by Boettcher and Wyllie (1969) in CaO-SiO_2-CO_2-H_2O and what was found in our study. Such a compositional barrier is possibly represented by aragonite + coesite, as experiments in Boettcher and Wyllie do not show saturation in silica, or by aragonite + coesite + grossular/zoisite, in the case we currently underestimate the Al-content of the liquids. All experiments performed in our study, at varying temperature, pressure, and water content do not show evidence for two coexisting vapor-liquid phases. Although this study was not designed to explicitly investigate the location of the second critical end point in CASHC, we speculate that experimental results suggest attainment of pressures at supercritical conditions.

Temperatures of 850 °C–900 °C at 4.2–6 GPa are predicted to occur in relatively warm subduction zones (Syracuse et al., 2010), e.g. in the Central American and northern Andean subduction zones, where deep-sea drilling sites have shown the presence of large masses of pelagic limestones. Hydrous carbonatitic liquids are therefore expected to be generated at the slab – mantle interface at sub-arc depth. Estimates of P-T paths from orogenic terrains (Penniston-Dorland et al., 2015) might suggest that warmer conditions are the rule rather than the exception, and 800 °C–900 °C at 4 GPa could be a common feature of subduction channels. If the pressure dependence of the dissolution of carbonates in the mobile phase is significantly larger than for silicates, as suggested qualitatively by our experiments (Figure 18.4) and by modeling of silica and $CaCO_3$ dissolution in aqueous fluids (Figure 18.5b), then liquids released by the slab are expected to shift from silicate rich to carbonatitic with increasing pressure. Hydrous carbonatitic liquids promote carbon scavenging from the slab, its transfer to the mantle wedge, and reaction with ultramafic rocks generating carbonated metasomatic wehrlites (Lee & Wyllie, 2000).

ACKNOWLEDGMENTS

This research was supported by the Italian Ministry of Education, University, and Research (MIUR) program PRIN2017 and by the Deep Carbon Observatory (DCO). We are greatly indebted to Andrea Risplendente for careful examination of run charges at the Electron Microprobe.

REFERENCES

Ague, J. J., & Nicolescu, S. (2014). Carbon dioxide released from subduction zones by fluid-mediated reactions. *Nature Geoscience*, *7*, 355–360.

Aiuppa, A., Fischer, T. P., Plank, T., Robidoux, P., & Di Napoli, R. (2017). Along-arc, inter-arc and arc-to-arc variations in volcanic gas CO_2/S_T ratios reveal dual source of carbon in arc volcanism. *Earth-Science Reviews*, *168*, 24–47.

Aubouin, J., von Huene, & the Shipboard Scientific Party (1982). Site 495: Cocos plate—Middle America Trench Outer Slope. *Initial Reports DSDP*, *67*, 79–141.

Boettcher, A. L., & Wyllie, P. J. (1969). The system $CaO\text{-}SiO_2\text{-}CO_2\text{-}H_2O$-III. Second critical end-point on the melting curve. *Geochimica et Cosmochimica Acta*, *33*, 611–632.

Brey, G. P., Girnis, A.V., Bulatov, V. K., Höfer, H. E., Gerdes, A., & Woodland, A. B. (2015). Reduced sediment melting at 7.5–12 GPa: Phase relations, geochemical signals and diamond nucleation. *Contribution to Mineralagoy and Petrology*, *170*, 1–25.

Caciagli, N. C., & Manning, C. E. (2003). The solubility of calcite in water at 6–16 kbar and 500–800 °C. *Contribution to Mineralogy and Petrology*, *146*, 275–285.

Cann, J. R., Langseth, M. G., Honnorez, J., Von Herzen, R. P., White, S. M., & the Shipboard Scientific Party (1983). 2. Sites 501 and 504: Sediments and ocean crust in an area of high heat flow on the southern flank of the Costa Rica Rift. *Initial Reports DSDP*, *69*, 31–173.

Carter, R. M., McCave, I. N., Richter, C., Carter, L., & the Shipboard Scientific Party (1999). 8. Site 1124: Rekohu drift—from the K/T boundary to the deep western boundary current. *Proceedings of the Ocean Drilling Program, Initial Reports*, *181*, 1–137.

Chou, I-M. (1986). Permeability of precious metals to hydrogen at 2 kb total pressure and elevated temperatures. *American Journal of Science*, *286*, 638–658.

Connolly, J.A.D. (1990). Multivariable phase diagrams: An algorithm based on generalized thermodynamics. *American Journal of Science*, *290*, 666–718.

Connolly, J.A.D., & Galvez, M. E. (2018). Electrolytic fluid speciation by Gibbs energy minimization and implications for subduction zone mass transfer. *Earth and Planetary Science Letters*, *501*, 90–102.

da Mommio, A. (2018). Evoluzione metamorfica delle unità paraderivate nella Finestra dei Tauri Occidentale (Ph.D. thesis, 216 p.). Università degli Studi di Milano.

Dasgupta, R., Hirschmann, M. M., & Withers, A. C. (2004). Deep global cycling of carbon constrained by the solidus of anhydrous, carbonated eclogite under upper mantle conditions. *Earth and Planetary Science Letters*, *227*, 73–85.

Dasgupta, R., & Hirschmann, M. M. (2006). Melting in the Earth's deep upper mantle caused by carbon dioxide. *Nature*, *440*, 659–662.

Donaldson, C. H. (1976). An experimental investigation of olivine morphology. *Contribution to Mineralogy and Petrology*, *57*, 187–213.

Facq, S., Daniel, I., Montagnac, G., Cardon, H., & Sverjensky, D. A. (2016). Carbon speciation in saline solutions in equilibrium with aragonite at high pressure. *Chemical Geology*, *431*, 44–53.

Ferri, F., Poli, S., & Rodríguez-Vargas, A. (2017). Andean volcanoes record carbonatite mantle metasomatism and CO_2 degassing at subduction zones. Paper presented at 27th Goldschmidt Conference, Paris.

Foustoukos, D. I., & Mysen, B. O. (2015). The structure of water-saturated carbonate melts. *American Mineralogist*, *100*, 35–46.

Franzolin, E., Schmidt, M. W., & Poli, S. (2011). Ternary Ca-Fe-Mg carbonates: Subsolidus phase relations at 3.5 GPa and a thermodynamic solid solution model including order/disorder. *Contribution to Mineralogy and Petrology*, *161*, 213–227.

Frezzotti, M. L., Selverstone, J., Sharp, Z. D., & Compagnoni, R. (2011). Carbonate dissolution during subduction revealed by diamond-bearing rocks from the Alps. *Nature Geoscience*, *4*, 703–706.

Garofalo, P. S. (2012). The composition of Alpine marine sediments (Bündnerschiefer Formation, W Alps) and the mobility of their chemical components during orogenic metamorphism. *Lithos*, *128–131*, 55–72.

Genge, M. J., Jones, A. P., & Price, G. D. (1995). An infrared and Raman study of carbonate glasses: Implications for the structure of carbonatite magmas. *Geochimica et Cosmochimica Acta*, *59*, 927–937.

Grassi, D., & Schmidt, M. W. (2011). The melting of carbonated pelites from 70 to 700 km depth. *Journal of Petrology*, *52*(4), 765–789.

Grice, J. D. (2005). The structure of spurrite, tilleyite and scawtite, and relationships to other silicate-carbonate minerals. *The Canadian Mineralogist*, *43*, 1489–1500.

Heirtzler, J.R., Veevers, J. J., Bolli, H. M., Carter, A. N., Cook, P. J., Krasheninnikov, V., et al., & the Shipboard Scientific Party (1974). 3. Site 260. *Initial Reports DSDP*, *27*, 89–127.

Holland, T., & Powell, R. (1991). A Compensated-Redlich-Kwong (CORK) equation for volumes and fugacities of CO_2 and H_2O in the range 1 bar to 50 kbar and 100–1600 °C. *Contribution to Mineralogy and Petrology*, *109*, 265–273.

Holland, T.J.B., & Powell, R. (2011). An improved and extended internally consistent thermodynamic dataset for phases of petrological interest, involving a new equation of state for solids. *Journal of Metamorphic Geology*, *29*, 333–383.

Huang, W. L., Wyllie, P. J., & Nehru, C. E. (1980). Subsolidus and liquidus phase relationships in the system $CaO\text{-}SiO_2\text{-}CO_2$ to 30 kbar with geological applications. *American Mineralogist*, *65*, 285–301.

Irving, A. J., & Wyllie, P. J. (1975). Subsolidus and melting relationships for calcite, magnesite and the join $CaCO_3\text{-}MgCO_3$ to 36 kb. *Geochimica et Cosmochimica Acta*, *39*, 35–53.

Kelemen, P. B., & Manning, C. E. (2015). Reevaluating carbon fluxes in subduction zones, what goes down, mostly comes up. *Proceedings of the National Academy of Sciences U.S.A.*, *112*, E3997–E4006.

Keppler, H. (2003). Water solubility in carbonatite melts. *American Mineralogist*, *88*, 1822–1824.

Kono, Y., Kenney-Benson, C., Hummer, D., Ohfuji, H., Park, C., Shen, G., et al. (2014). Ultralow viscosity of carbonate melts at high pressures. *Nature Communications*, *5*, 1–8.

Lee, W. J., & Wyllie, P. J. (2000). The system CaO-MgO-SiO_2-CO_2 at 1 GPa, metasomatic wehrlites, and primary carbonatite magmas. *Contribution to Mineralogy and Petrology*, *138*, 214–228.

Liu, L-g., & Lin, C-C. (1995). High-pressure phase transformations of carbonates in the system CaO-MgO-SiO_2-CO_2. *Earth and Planetary Science Letters*, *134*, 297–305.

Lofgren, G. (1974). An experimental study of plagioclase crystal morphology: Isothermal crystallization. *American Journal of Science*, *274*, 243–273.

Manning, C. E. (1994). The solubility of quartz in H_2O in the lower crust and upper mantle. *Geochimica et Cosmochimica Acta*, *58*, 4831–4839.

Manning, C. E., Shock, E. L., & Sverjensky, D. A. (2013). The chemistry of carbon in aqueous fluids at crustal and upper-mantle conditions: Experimental and theoretical constraints. *Reviews in Mineralogy & Geochemistry*, *75*, 109–148.

Minarik, W. G., & Watson, E. B. (1995). Interconnectivity of carbonate melt at low melt fraction. *Earth and Planetary Science Letters*, *133*, 423–437.

Paterson, M. S. (1958). The melting of calcite in the presence of water and carbon dioxide. *American Mineralogist*, *43*, 603–606.

Penniston-Dorland, S. C., Kohn, M. J., & Manning, C. E. (2015). The global range of subduction zone thermal structures from exhumed blueschists and eclogites: Rocks are hotter than models. *Earth and Planetary Science Letters*, *428*, 243–254.

Plank, T. (2014). The chemical composition of subducting sediments. In K. Turekian & H. Holland (Eds.), *Treatise on Geochemistry* (2nd ed., vol. 4, pp. 607–629). Elsevier.

Plank, T., & Langmuir, C. H. (1998). The chemical composition of subducting sediment and its consequences for the crust and mantle. *Chemical Geology*, *145*, 325–394.

Poli, S. (2015). Carbon mobilized at shallow depths in subduction zones by carbonatitic liquids. *Nature Geoscience*, *8*, 633–636.

Poli, S., (2016). Melting carbonated epidote eclogites: Carbonatites from subducting slabs. *Progress in Earth and Planetary Science 3*, 27.

Poli, S., & Schmidt, M. W. (1998). The high-pressure stability of zoisite and phase relationships of zoisite-bearing assemblages. *Contribution to Mineralogy and Petrology*, *130*, 162–175.

Schmidt, M. W., & Poli, S. (2014). Devolatilization during subduction. In K. Turekian & H. Holland (Eds.), *Treatise on Geochemistry* (2nd ed., vol. *4*, pp. 669–701). Elsevier.

Skora, S., Blundy, J. D., Brooker, R. A., Green, E.C.R., De Hoog, J.C.M., & Connolly, J.A.D. (2015). Hydrous phase relations and trace element partitioning behaviour in calcareous sediments at subduction-zone conditions. *Journal of Petrology*, *56*(5), 953–980.

Sokol, A. G., Kupriyanov, I. N., & Palyanov, Y. N. (2013). Partitioning of H_2O between olivine and carbonate-silicate melts at 6.3 GPa and 1400 °C: Implications for kimberlite formation. *Earth and Planetary Science Letters*, *383*, 58–67.

Susaki, J., Akaogi, M., Akimoto, S. & Shinomura, O. (1985). Garnet perovskite transformation in $CaGeO_3$: *In situ* X-ray measurements using synchrotron radiation. *Geophysical Research Letters*, *12*, 729–732.

Syracuse, E. M., Van Keken, P. E., & Abers, G. A. (2010). The global range of subduction zone thermal models. *Physics of the Earth and Planetary Interiors*, *183*, 73–90.

Taylor, L. A., Logvinova, A. M., Howarth, G. H., Liu, Y., Peslier, A. H., Rossman, G. R., et al. (2016). Low water contents in diamond mineral inclusions: Proto-genetic origin in a dry cratonic lithosphere. *Earth and Planetary Science Letters*, *433*, 125–132.

Thomsen, T. B., & Schmidt, M. W. (2008). Melting of carbonated pelites at 2.5–5.0 GPa, silicate-carbonatite liquid immiscibility, and potassium-carbon metasomatism of the mantle. *Earth and Planetary Science Letters*, *267*, 17–31.

Tsuno, K., & Dasgupta, R. (2012). The effect of carbonates on near-solidus melting of pelite at 3 GPa: Relative efficiency of H_2O and CO_2 subduction. *Earth and Planetary Science Letters*, *319–320*, 185–196.

Tumiati, S., Tiraboschi, C., Sverjensky, D. A., Pettke, T., Recchia, S., Ulmer, P., et al. (2017). Silicate dissolution boosts the CO_2 concentrations in subduction fluids. *Nature Communications*, *8*, 616.

von der Borch, C.C., and the Shipboard Scientific Party. (1974). Site 212. *Initial Reports DSDP*, *22*, 37–83.

Watson, E. B., Brenan, J. M., & Baker, D. R. (1990). Distribution of fluids in the continental lithospheric mantle. In M. A. Menzies (Ed.), *The Continental Lithospheric Mantle* (pp. 111–125). Oxford: Clarendon.

Wyllie, P. J., & Boettcher, A. L. (1969). Liquidus phase relationships in the system CaO-CO_2-H_2O to 40 kilobars pressure with petrological applications. *American Journal of Science*, *267-A*, 489–508.

Wyllie, P. J., & Tuttle, O. F. (1959). Melting of calcite in presence of water. *American Mineralogist*, *44*, 453–461.

Wyllie, P. J., & Tuttle, O. F. (1960). The system CaO-CO_2-H_2O and the origin of carbonatites. *Journal of Petrology*, *1*, 1–46.

Zhang, J., Li, B., Utsumi, W., & Liebermann, R. C. (1996). *In situ* X-ray observations on the coesite stishovite transition: Reversed phase boundary and kinetics. *Physics and Chemistry of Minerals*, *23*, 1–10.

Zhao, S., Schettino, E., Merlini, M., & Poli, S. (2019). The stability and melting of aragonite: An experimental and thermodynamic model for carbonated eclogites in the mantle. *Lithos*, *324–325*, 105–114.